Metallic and Insulating Phases of Repulsively Interacting Fermions in a 3D Optical Lattice

U. Schneider, *et al.*

Science **322**, 1520 (2008);
DOI: 10.1126/science.1165449

of most monolithic structural ceramics with engineered grain boundaries, i.e., coarse-grained Al_2O_3, Si_3N_4, and SiC (*35*–*42*). However, the contribution from bridging alone does not explain why the observed toughness of the best brick-and-mortar 80% alumina structure (J_c ~ 8000 J/m^2) is more than 300 times higher in terms of energy than the toughness of its main constituent, Al_2O_3 (J_c ~ 26 J/m^2). We believe that of the various hybrid materials that we have fabricated, this structure best mimics nacre. Freeze casting followed by pressing and a second sintering stage results in a microstructure with high ceramic contents characterized by the submicrometer lubricating polymer interlayers between ceramic "bricks" (deformation and micrometer-scale tearing in these interlayers can be seen in Fig. 4A); combined with the roughness of the ceramic interfaces and the presence of stiff ceramic bridges between grains with micrometer and submicrometer dimensions (Fig. 1, C and D), this method promotes controlled sliding and "sliding interference" (Fig. 4) between the rough ceramic interlayers, thereby enhancing the toughness through extremely efficient energy dissipation. The result is synthetic materials that, like nacre and bone, are far tougher than what could be expected from the simple mixture of their constituents (Fig. 5A).

Concluding remarks and future challenges. A better appreciation of the unique mechanical properties of these freeze-cast composites can be gained by comparing them to other materials. By combining two relatively ordinary phases, i.e., a hard yet brittle ceramic with a relatively soft (in comparison) polymer, we have synthesized primarily (ceramic) alumina hybrid structures with specific strength and toughness properties that match those of engineering (metallic) aluminum alloys (Fig. 5B) and moreover display a higher stiffness. This has been made possible through the development of hierarchical architectures that combine toughening mechanisms acting at multiple scales, from submicrometer dimensions (i.e., the ceramic bridges between lamellae or bricks or the inelastic polymer deformation) and higher. These results highlight the tremendous potential of the biomimetic approach and suggest promising strategies for structural optimization. In particular, a key attribute of nacre has been extremely difficult to replicate: The structure consists of 95 vol. % ceramic with very little of the organic soft phase, which is distributed as a thin (2 to 3 nm) protein film that acts like a lubricant. At present, our materials contain too much of the soft phase, and our ceramic layer thicknesses are still somewhat coarse in comparison to nacre; indeed, a reduction in the polymer content and refinement of the ceramic layers should improve strength and provide additional nanoscale toughening mechanisms similar to those acting in natural materials. In this regard, our current studies are focused on the development of these hybrid structures with much higher inorganic content, the manipulation of the properties of the soft lubricating phase, and extending this concept to other material combinations, principally metal-infiltrated ceramics.

References and Notes

1. G. Mayer, *Science* **310**, 1144 (2005).
2. M. A. Meyers, P. Y. Chen, A. Y. M. Lin, Y. Seki, *Prog. Mater. Sci.* **53**, 1 (2008).
3. C. Ortiz, M. C. Boyce, *Science* **319**, 1053 (2008).
4. J. Aizenberg *et al*., *Science* **309**, 275 (2005).
5. F. Barthelat, H. D. Espinosa, *Exp. Mech.* **47**, 311 (2007).
6. R. K. Nalla, J. H. Kinney, R. O. Ritchie, *Biomaterials* **24**, 3955 (2003).
7. R. K. Nalla, J. J. Kruzic, J. H. Kinney, R. O. Ritchie, *Biomaterials* **26**, 217 (2005).
8. R. O. Ritchie, *Mater. Sci. Eng. A* **103**, 15 (1988).
9. R. Z. Wang, Z. Suo, A. G. Evans, N. Yao, I. A. Aksay, *J. Mater. Res.* **16**, 2485 (2001).
10. A. G. Evans *et al*., *J. Mater. Res.* **16**, 2475 (2001).
11. X. D. Li, W. C. Chang, Y. J. Chao, R. Z. Wang, M. Chang, *Nano Lett.* **4**, 613 (2004).
12. B. L. Smith *et al*., *Nature* **399**, 761 (1999).
13. F. Song, A. K. Soh, Y. L. Bai, *Biomaterials* **24**, 3623 (2003).
14. H. M. Chan, *Annu. Rev. Mater. Sci.* **27**, 249 (1997).
15. J. S. Moya, *Adv. Mater.* **7**, 185 (1995).
16. A. Sellinger *et al*., *Nature* **394**, 256 (1998).
17. Z. Tang, N. A. Kotov, S. Magonov, B. Ozturk, *Nat. Mater.* **2**, 413 (2003).
18. L. J. Bonderer, A. R. Studart, L. J. Gauckler, *Science* **319**, 1069 (2008).
19. P. Podsiadlo *et al*., *Science* **318**, 80 (2007).
20. S. Deville, E. Saiz, R. K. Nalla, A. P. Tomsia, *Science* **311**, 515 (2006).
21. S. Deville, E. Saiz, A. P. Tomsia, *Acta Mater.* **55**, 1965 (2007).
22. T. Fukasawa, M. Ando, T. Ohji, S. Kanzaki, *J. Am. Ceram. Soc.* **84**, 230 (2001).
23. T. Fukasawa, Z. Y. Deng, M. Ando, T. Ohji, Y. Goto, *J. Mater. Sci.* **36**, 2523 (2001).
24. K. Araki, J. W. Halloran, *J. Am. Ceram. Soc.* **87**, 1859 (2004).
25. K. J. Koester, J. W. Ager, R. O. Ritchie, *Nat. Mater.* **7**, 672 (2008).
26. A. Tasdemirci, I. W. Hall, B. A. Gama, M. Guiden, *J. Compos. Mater.* **38**, 995 (2004).
27. D. R. Johnson, X. F. Chen, B. F. Oliver, R. D. Noebe, J. D. Whittenberger, *Intermetallics* **3**, 99 (1995).
28. R. M. Jones, *Mechanics of Composite Materials* (Taylor & Francis, Philadelphia, PA, ed. 2, 1999).
29. Supporting online material on *Science* Online.
30. J. K. Shang, R. O. Ritchie, *Metallurg. Trans. A* **20**, 897 (1989).
31. Instead of crack extension being solely associated with the main crack tip growing forward, crack advance also can occur by microcracks (or other damage) initiated ahead of the main crack tip linking back to the tip.
32. J. Cook, C. C. Evans, J. E. Gordon, D. M. Marsh, *Proc. R. Soc. Lond. A Math. Phys. Sci.* **282**, 508 (1964).
33. L. S. Sigl, P. A. Mataga, B. J. Dalgleish, R. M. McMeeking, A. G. Evans, *Acta Metall.* **36**, 945 (1988).
34. A. Y. M. Lin, P. Y. Chen, M. A. Meyers, *Acta Biomater.* **4**, 131 (2008).
35. P. F. Becher *et al*., *J. Am. Ceram. Soc.* **81**, 2821 (1998).
36. J. J. Cao, W. J. MoberlyChan, L. C. DeJonghe, C. J. Gilbert, R. O. Ritchie. *J. Am. Ceram. Soc.* **79**, 461 (1996).
37. J. J. Kruzic, R. M. Cannon, R. O. Ritchie, *J. Am. Ceram. Soc.* **87**, 93 (2004).
38. J. J. Kruzic, R. M. Cannon, R. O. Ritchie, *J. Am. Ceram. Soc.* **88**, 2236 (2005).
39. F. F. Lange, *J. Am. Ceram. Soc.* **56**, 518 (1973).
40. Y. W. Mai, B. R. Lawn, *J. Am. Ceram. Soc.* **70**, 289 (1987).
41. N. P. Padture, B. R. Lawn, *J. Am. Ceram. Soc.* **77**, 2518 (1994).
42. P. L. Swanson, C. J. Fairbanks, B. R. Lawn, Y. W. Mai, B. J. Hockey, *J. Am. Ceram. Soc.* **70**, 279 (1987).
43. U. G. K. Wegst, M. F. Ashby, *Philos. Mag.* **84**, 2167 (2004).

44. This work was supported by the Director, Office of Science, Office of Basic Energy Sciences, Division of Materials Sciences and Engineering, of the U.S. Department of Energy under Contract No. DE-AC02-05CH11231

Supporting Online Material

www.sciencemag.org/cgi/content/full/322/5907/1516/DC1
Materials and Methods
Figs. S1 and S2
References

19 August 2008; accepted 21 October 2008
10.1126/science.1164865

Metallic and Insulating Phases of Repulsively Interacting Fermions in a 3D Optical Lattice

U. Schneider,[1] L. Hackermüller,[1] S. Will,[1] Th. Best,[1] I. Bloch,[1,2]* T. A. Costi,[3] R. W. Helmes,[4] D. Rasch,[4] A. Rosch[4]

The fermionic Hubbard model plays a fundamental role in the description of strongly correlated materials. We have realized this Hamiltonian in a repulsively interacting spin mixture of ultracold ^{40}K atoms in a three-dimensional (3D) optical lattice. Using in situ imaging and independent control of external confinement and lattice depth, we were able to directly measure the compressibility of the quantum gas in the trap. Together with a comparison to ab initio dynamical mean field theory calculations, we show how the system evolves for increasing confinement from a compressible dilute metal over a strongly interacting Fermi liquid into a band-insulating state. For strong interactions, we find evidence for an emergent incompressible Mott insulating phase. This demonstrates the potential to model interacting condensed-matter systems using ultracold fermionic atoms.

Interacting fermions in periodic potentials lie at the heart of condensed-matter physics, presenting some of the most challenging problems to quantum many-body theory. A prominent example is high-temperature superconductivity in cuprate compounds (*1*). An essential part of the physics in these systems is described by the fermionic Hubbard Hamiltonian (*2*), which models interacting electrons in a periodic potential (*1*, *3*). In a real solid, however, the effects of interest are typically complicated by, for example, multiple bands, impurities, and the long-range nature of Coulomb interactions, which becomes especially relevant close to a metal-to-insulator transition.

Probing this Hamiltonian in a controllable and clean experimental setting is therefore of great importance. Ultracold atoms in optical lattices provide such a defect-free system (*4*, *5*), in which the relevant parameters can be independently controlled, thus allowing quantitative comparisons of the experiment with modern quantum many-body theories. For the case of bosonic particles (*6*, *7*), the importance of ultracold quantum gases in this respect has been shown in a series of experiments on the superfluid–to–Mott insulator transition (*8*–*10*). For both bosonic and fermionic systems, the entrance into a Mott insulating state is signaled by a vanishing compressibility, which can in principle be probed experimentally by testing the response of the system to a change in external confinement. This is a straightforward way to identify the interaction-induced Mott insulator and to distinguish it, for instance, from a disorder-induced Anderson insulator (*11*–*13*). In a solid, however, the corresponding compressibility can usually not be measured directly, because a compression of the crystalline lattice by an external force does not change the number of electrons per unit cell [see supporting online material (*14*)].

We have studied noninteracting and repulsively interacting spin mixtures of fermionic atoms deep in the degenerate regime in a three-dimensional (3D) optical lattice, where the interaction strength, the lattice depth, and the external harmonic confinement of the quantum gas can be varied independently. By monitoring the in-trap density distribution for increasing harmonic confinement, we directly probed the compressibility of the many-body system. This measurement allows us to clearly distinguish compressible metallic phases from globally incompressible states and reveals the strong influence of interactions on the density distribution. Additionally, we measured the fraction of atoms on doubly occupied lattice sites for different experimental parameters to probe the local onsite physics of the system. In previous experiments, a suppression of the number of doubly occupied sites was demonstrated for increasing interaction strength for bosons (*15*) and fermions (*16*) at fixed harmonic confinement, signaling the entrance into a strongly interacting regime.

We compare the experimentally observed density distributions and fractions of doubly occupied sites to numerical calculations, using dynamical mean field theory (DMFT) (*17*–*20*). DMFT is a central method of solid-state theory being widely used to obtain ab initio descriptions of strongly correlated materials (*18*). The comparison of DMFT predictions with experimental results on ultracold fermions in optical lattices constitutes a parameter-free experimental test of the validity of DMFT in a 3D system.

Theoretical model. Restricting our discussion to the lowest-energy band of a simple cubic 3D optical lattice, the fermionic quantum gas mixture can be modeled via the Hubbard Hamiltonian (*2*), with an additional term describing the underlying harmonic potential

$$\hat{H} = -J \sum_{\langle i,j\rangle,\sigma} \hat{c}^{\dagger}_{i,\sigma}\hat{c}_{j,\sigma} + U\sum_i \hat{n}_{i,\downarrow}\hat{n}_{i,\uparrow} + V_t\sum_i (i_x^2 + i_y^2 + \gamma^2 i_z^2)(\hat{n}_{i,\downarrow} + \hat{n}_{i,\uparrow}) \quad (1)$$

Here the indices i, j denote different lattice sites in the 3D system [$i = (i_x, i_y, i_z)$], $\langle i, j\rangle$ neighboring lattice sites, $\sigma \in \{\downarrow,\uparrow\}$ the two different spin states, J the tunneling matrix element, and U the effective onsite interaction. The operators $\hat{c}_{i,\sigma}$ are the annihilation operators of a fermion in spin state σ on the ith lattice site, $\hat{c}^{\dagger}_{i,\sigma}$ are the creation operators, and $\hat{n}_{i,\sigma}$ measures the corresponding atom number. The strength of the harmonic confinement is parameterized by the energy offset $V_t = \frac{1}{2}m\omega_{\perp}^2 d^2$ between two adjacent lattice sites at the trap center, with $\omega_{\perp} = \omega_x = \omega_y \neq \omega_z$ being the horizontal trap frequency, d the lattice constant, and m the mass of a single atom. The constant aspect ratio of the trap is denoted by $\gamma = \omega_z/\omega_{\perp}$. Because of the Pauli principle, every lattice site can be occupied by at most one atom per spin state.

The quantum phases of the Hubbard model with harmonic confinement are governed by the interplay between three energy scales: kinetic energy, whose scale is given by the lattice bandwidth $12J$; interaction energy U; and the strength of the harmonic confinement, which can conveniently be expressed by the characteristic trap energy $E_t = V_t[\gamma N_\sigma/(4\pi/3)]^{2/3}$, which denotes the Fermi energy of a noninteracting cloud in the zero-tunneling limit, with N_σ being the number of atoms per spin state ($N_\downarrow = N_\uparrow$). The characteristic trap energy depends on both atom number and trap frequency via $E_t \propto \omega_{\perp}^2 N_\sigma^{2/3}$ and describes the effective compression of the quantum gas, controlled by the trapping potential in the experiment.

Depending on which term in the Hamiltonian dominates, different kinds of many-body ground states can occur in the trap center (Fig. 1). For weak interactions in a shallow trap, $U << E_t << 12J$, the Fermi energy is smaller than the lattice bandwidth ($E_F < 12J$), and the atoms are delocalized in order to minimize their kinetic energy. This leads to compressible metallic states with central filling $n_{0,\sigma} < 1$, where the local filling factor $n_{i,\sigma} = \langle \hat{n}_{i,\sigma}\rangle$ denotes the average occupation per spin state of a given lattice site. A dominating repulsive interaction $U >> 12J$ and $U >> E_t$ suppresses the double occupation of lattice sites and can lead to Fermi liquid ($n_{0,\sigma} < 1/2$) or Mott insulating ($n_{0,\sigma} = 1/2$) states at the trap center, depending on the ratio of kinetic energy to characteristic trap energy. Stronger compressions lead to higher filling factors, ultimately ($E_t >> 12J$, $E_t >> U$) resulting in an incompressible band insulator with unity central filling at zero temperature ($T = 0$).

Finite temperature reduces all filling factors and enlarges the cloud size, because the system needs to accommodate the corresponding entropy. Furthermore, in the trap the filling always varies

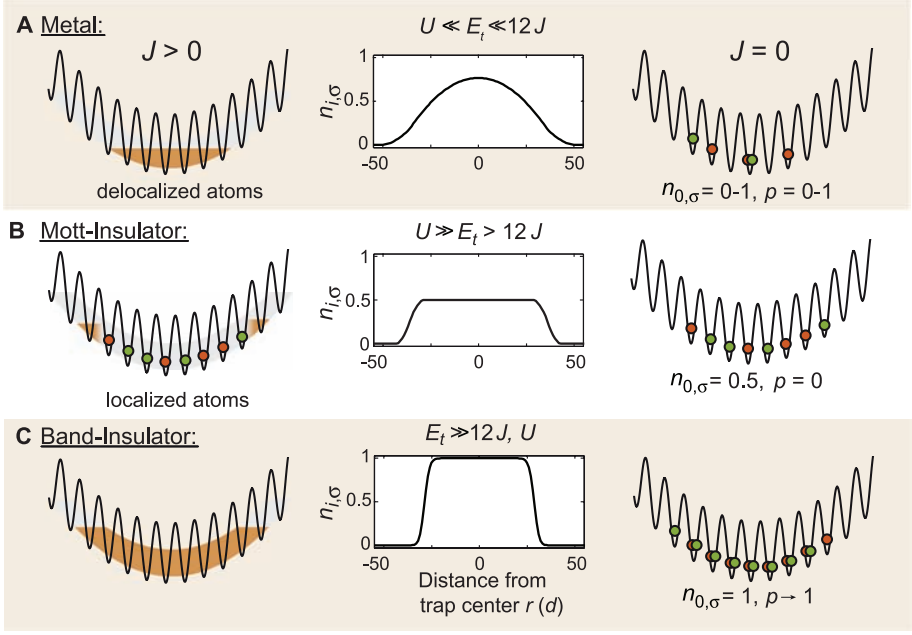

Fig. 1. (**A** to **C**) Relevant phases of the Hubbard model with an inhomogeneous trapping potential for a spin mixture at $T = 0$. A schematic is shown in the left column. The center column displays the corresponding in-trap density profiles, and the right column outlines the distribution of singly and doubly occupied lattice sites after a rapid projection into the zero tunneling limit, with p denoting the total fraction of atoms on doubly occupied lattice sites.

[1]Institut für Physik, Johannes Gutenberg-Universität, 55099 Mainz, Germany. [2]Max-Planck-Institut für Quantenoptik, 85748 Garching, Germany. [3]Institut für Festkörperforschung and Institute for Advanced Simulation, Forschungszentrum Jülich, 52425 Jülich, Germany. [4]Institut für Theoretische Physik, Universität zu Köln, 50937 Cologne, Germany.

*To whom correspondence should be addressed. E-mail: bloch@uni-mainz.de

smoothly from a maximum at the center to zero at the edges of the cloud. For a dominating trap and strong repulsive interaction at low temperature ($E_t > U > 12J$), the interplay between the different terms in the Hamiltonian gives rise to a wedding cake–like structure (Fig. 4, E and F) consisting of a band-insulating core ($n_{0,\sigma} \approx 1$) surrounded by a metallic shell ($1/2 < n_{i,\sigma} < 1$), a Mott insulating shell ($n_{i,\sigma} = 1/2$), and a further metallic shell ($n_{i,\sigma} < 1/2$) (*19*). The outermost shell always remains metallic, independent of interaction and confinement; only its thickness varies (figs. S7 and S8).

Experimental setup. We used an equal mixture of quantum degenerate fermionic ^{40}K atoms in the two hyperfine states $|F, m_F\rangle = |\frac{9}{2}, -\frac{9}{2}\rangle \equiv |\downarrow\rangle$ and $|\frac{9}{2}, -\frac{7}{2}\rangle \equiv |\uparrow\rangle$ in a pancake-shaped optical dipole trap (aspect ratio $\gamma \approx 4$), which was formed by overlapping two elliptical laser beams (wavelength $\lambda = 1030$ nm) traveling in the horizontal plane (*14*). Through evaporative cooling, final temperatures of $T/T_F = 0.15(3)$ with 1.5×10^5 to 2.5×10^5 potassium atoms were reached. The temperature was extracted from time-of-flight images by means of Fermi fits. A Feshbach resonance located at a magnetic field $B = 202.1$ G (*21*) was used to tune the scattering length a between the two spin states and thereby control the onsite interaction U. The creation of the spin mixture and the last evaporation step were performed either above the resonance (220 G), giving access to non-interacting (209.9 G) and repulsively interacting clouds with $a \leq 150\, a_0$ (where a_0 denotes the Bohr radius), or below the resonance (165 G), where larger scattering lengths up to $a = 300\, a_0$ (191.3 G) can be reached. A further approach to the Feshbach resonance was hindered by enhanced losses and heating in the lattice (*22*).

After evaporation, the magnetic field was tuned to the desired value. Subsequently, a blue-detuned 3D optical lattice ($\lambda_{lat} = 738$ nm) with simple cubic symmetry was increased to a potential depth of $V_{lat} = 1\, E_r$, where $E_r = h^2/(2m\lambda_{lat}^2)$ denotes the recoil energy.

The combination of a red-detuned dipole trap and a blue-detuned lattice potential allows us to vary lattice depth and external confinement independently. In this way, a wide range of horizontal trap frequencies can be accessed [$\omega_\perp \simeq 2\pi \times (20 - 120)$Hz], especially enabling metallic states with high atom numbers. To monitor the in situ density distribution for different external confinements, we ramped the dipole trap depth in 100 ms to the desired external harmonic confinement, followed by a linear increase of the optical lattice depth to $V_{lat} = 8\, E_r$ within 50 ms. An in situ image of the cloud was taken along the short (vertical) axis of the trap using phase-contrast imaging (*23*) at detunings of $\Delta = 2\pi \times (200 - 330)$ MHz after a hold time of 12 ms in the lattice. From this picture, the cloud size $R = \sqrt{\langle r_\perp^2 \rangle}$ was extracted by means of adapted 2D Fermi fits (fig. S6). Because phase-contrast imaging modifies the state of the atoms only marginally, the quasi-momentum distribution can be measured in the same experimental run with a band-mapping technique (*24*–*26*). For this, the lattice is ramped down in 200 μs and a standard absorption image is taken after 10 ms time of flight.

All experimental data were compared to numerical calculations, in which the DMFT equations of the homogeneous model were solved for a wide range of temperatures and chemical potentials using a numerical renormalization group approach (*14*) (*27*, *28*). The trapped system can be approximated to very high accuracy by the uniform system through a local density approximation (LDA), even close to the boundary between a metal and an insulator (*19*, *29*). For a

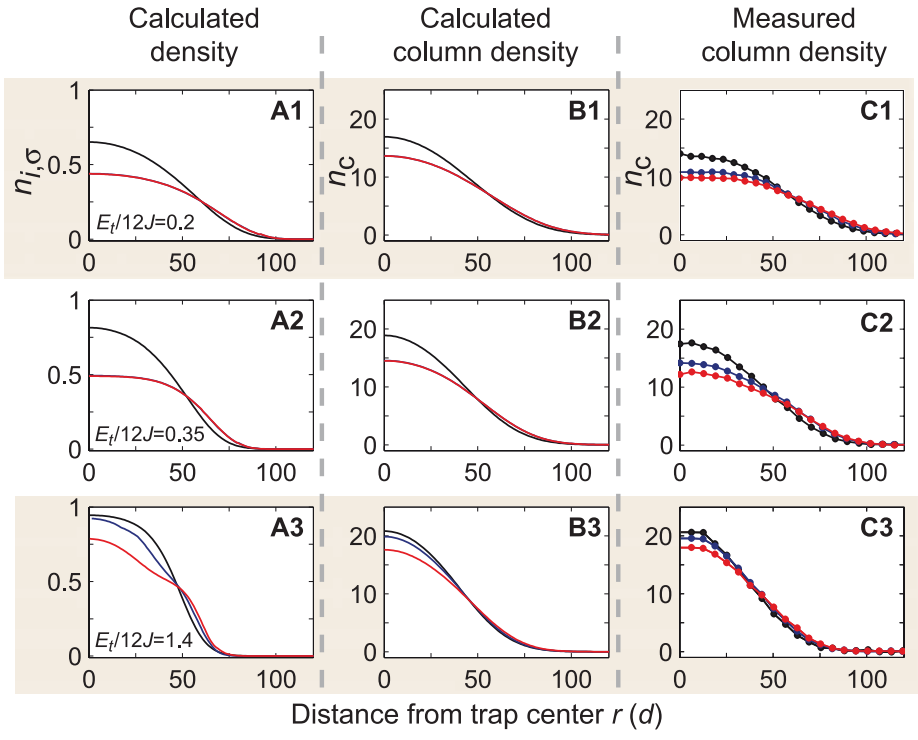

Fig. 2. Comparison of in-trap density profiles. Calculated radial density profiles for different compressions (harmonic confinements) $E_t/12J$ (left column, **A1** to **A3**), corresponding column densities obtained after integration over the z axis and convolution with the point spread function (*14*) of our imaging system (center column, **B1** to **B3**), and experimental results (azimuthally averaged over more than five shots) (**C1** to **C3**) for three different interaction strengths $U/12J = 0$ (black), $U/12J = 1$ (blue), and $U/12J = 1.5$ (red). At small compressions [(A) and (B)], the calculated density profiles for $U/12J = 1$ and $U/12J = 1.5$ are indistinguishable, because in both cases double occupations are almost completely suppressed for $n_{i,\sigma} < 1/2$.

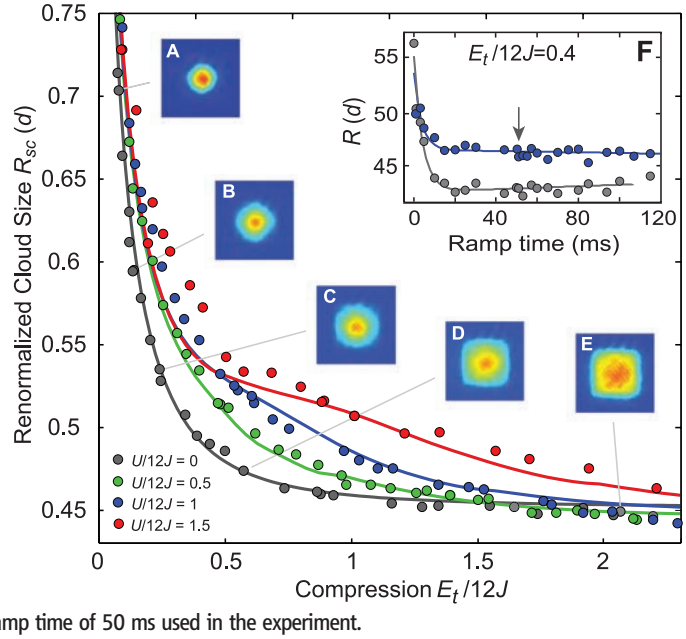

Fig. 3. Cloud sizes of the interacting spin mixture versus compression. Measured cloud size R_{sc} in a $V_{lat} = 8\, E_r$ deep lattice as a function of the external trapping potential for various interactions $U/12J = 0 \ldots 1.5$ is shown. Dots denote single experimental shots, lines denote the theoretical expectation from DMFT for an initial temperature $T/T_F = 0.15$. The insets **(A** to **E)** show the quasi-momentum distribution of the noninteracting clouds (averaged over several shots). **(F)** Resulting cloud size for different lattice ramp times at $E_t/12J = 0.4$ for a noninteracting and an interacting Fermi gas. The arrow marks the ramp time of 50 ms used in the experiment.

comparison with the experimental results, it is convenient to express the cloud size R in rescaled units $R_{sc} = R/(\gamma N_\sigma)^{1/3}$, along with the dimensionless compression $E_t/12J$. In these units, the cloud size depends only on the interaction strength $U/12J$ and the entropy. In all calculations, we used the entropy determined from a noninteracting Fermi gas in a harmonic trap at an initial temperature T/T_F and assumed adiabatic lattice loading.

Cloud compression. The numerically calculated density distributions, the corresponding column densities, and the experimentally measured ones are presented in Fig. 2. Whereas for low compression all distributions are metallic (the first row), we find a Mott insulating core with half filling at intermediate compression and strong repulsion (the second row). For high compression, the noninteracting curve shows a band-insulating core and the repulsive curves display a metallic core. In order to compare experiment and theory quantitatively, the measured cloud size R_{sc} and the numerically calculated one are plotted in Fig. 3 as a function of the characteristic trap energy E_t. Additionally, the global compressibility $\kappa_{R_{sc}} = -\frac{1}{R_{sc}^3}\frac{\partial R_{sc}}{\partial(E_t/12J)}$ (Fig. 4 and fig. S2) of the system can be extracted from these measurements by means of linear fits to four consecutive data points to determine the derivative. In the noninteracting case, we find the cloud sizes (Fig. 3, black dots) to decrease continuously with compression until the characteristic trap energy roughly equals the lattice bandwidth ($E_t/12J \sim 1$). For stronger confinement, the compressibility approaches zero (Fig. 4A), because almost all atoms are in the band-insulating regime while the surrounding metallic shell becomes negligible. The corresponding quasi-momentum distribution (Fig. 3, A to E) changes gradually from a partially filled first Brillouin zone, characteristic for a metal, to an almost evenly filled first Brillouin zone for increasing compressions, as expected for a band insulator. However, a band-mapping technique reveals only the relative occupations of the extended Bloch states. For an inhomogeneous system, it therefore provides no information about the real-space density and especially cannot distinguish insulating from compressible states; for instance nonequilibrium states in which the atomic wavefunctions are localized to single lattice sites. In contrast, the measurements shown here directly demonstrate the incompressibility of the fermionic band insulator, in excellent agreement with the theoretical expectation for a noninteracting Fermi gas (Fig. 4A, black line).

For moderately repulsive interactions ($U/12J$ = 0.5, 1) (Fig. 3, green and blue lines), the cloud size is clearly bigger than in the noninteracting case but eventually reaches the size of the band insulator. For stronger repulsive interactions ($U/12J$ = 1.5) (Fig. 3B, red line), we find the onset of a region ($0.5 < E_t/12J < 0.7$) where the cloud size decreases only slightly with increasing harmonic confinement, whereas for stronger confinements the compressibility increases again. This is consistent with the formation of an incompressible Mott insulating core, surrounded by a compressible metallic shell, as can be seen in the corresponding in-trap density profiles (Fig. 4, E and F). For higher confinements, an additional metallic core ($1/2 < n_{i,\sigma} < 1$) starts to form in the center of the trap and the cloud size decreases again. A local minimum in the global compressibility is in fact a genuine characteristic of a Mott insulator, and for large U and low T, we expect the global compressibility in the middle of the Mott region to vanish as $1/U^2$ (fig. S1). The experimental data, indeed, show an indication of this behavior (Fig. 4 C) for increasing interactions. For $E_t/12J \simeq 0.5$, a minimum in the compressibility is observed, followed by an increase of the compressibility around $E_t/12J \simeq 0.8$, slightly earlier than predicted by theory.

When the system is compressed even further, all cloud sizes approach that of a band-insulating state and all compressibilities tend to zero. In the theory predictions, the repulsively interacting clouds can even become slightly smaller than the noninteracting ones because of Pomeranchuk cooling (*30*): At the same average entropy per particle, the interacting system has a considerably lower temperature in the lattice, because the spin entropy is enhanced because of interactions (fig. S4). In the experiment, this feature is barely visible, because a second effect becomes important: At very high compressions ($E_t/12J \gtrsim 2$), the second Bloch band gets slightly populated during the lattice ramp-up, which leads to smaller cloud sizes for all interactions, because a small number of atoms in a nearly empty band can carry a considerable amount of entropy.

Overall, we find the measured cloud sizes to be in very good quantitative agreement with the theoretical calculations up to $U/12J$ = 1.5 (B = 175 G). Nevertheless, for repulsive interactions and medium compression ($E_t/12J \approx 0.5$), the cloud size is slightly bigger than the theoretical expectation. The discrepancies become more prominent for stronger interactions; that is, on further increasing the scattering length. This could be

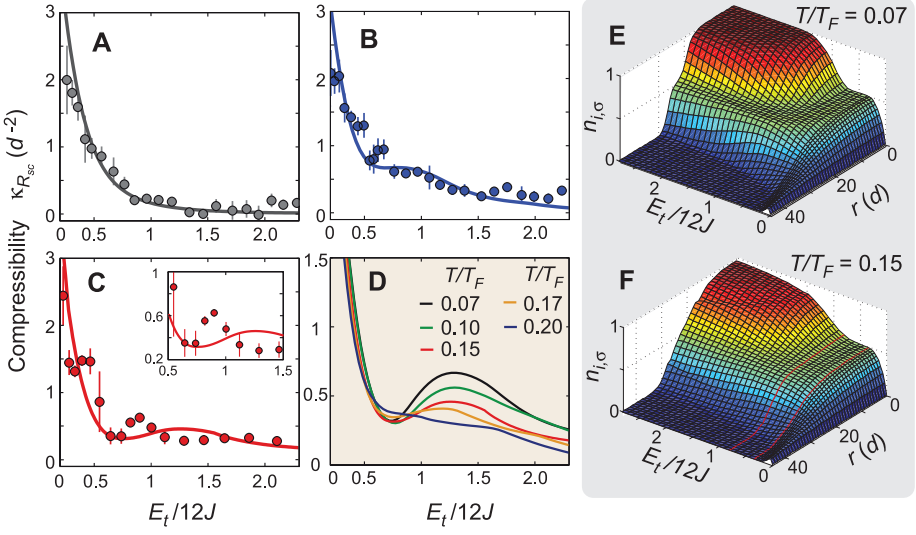

Fig. 4. Compressibility and in-trap density distribution. (**A** to **C**) Global compressibility $\kappa_{R_{sc}}$ of the atom cloud for various interactions [(A) $U/12J = 0$, (B) $U/12J = 1$, (C) $U/12J = 1.5$]. Dots denote the result of linear fits on the measured data, and the error bars represent the fit uncertainty. Solid lines display the theoretically expected results for an initial temperature $T/T_F = 0.15$. The influence of the initial temperature on the calculated compressibility is shown in (**D**) for $U/12J = 1.5$. The corresponding density distributions are plotted in (**E**) and (**F**), with r denoting the distance to the trap center (see also figs. S7 and S8). The red lines mark the region where a Mott insulating core has formed and the global compressibility is reduced.

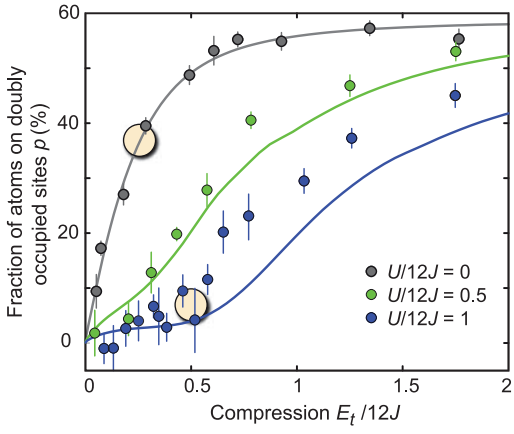

Fig. 5. Fraction of atoms on doubly occupied sites versus compression for different interaction strengths $U/12J$ = 0...1. The yellow circles indicate the fraction of atoms on doubly occupied sites for a constant cloud size $R_{sc} = 0.53$ (Fig. 3). The error bars denote the SD of at least four measurements.

caused by nonequilibrium dynamics in the formation of a Mott insulating state for strong interactions or may be an effect not covered by the simple single-band Hubbard model (*30*) or the DMFT calculations and requires further investigation.

To ensure that the lattice loading time of 50 ms was adiabatic, we measured the resulting in situ cloud size as a function of ramp time (Fig. 3F) in the regime around $E_t/12J \approx 0.5$, where the differences between experiment and theory are most pronounced. In this regime, a too-rapid loading would result in a larger cloud, and our measurement therefore indicates adiabaticity for the ramp time used. However, a second, longer time scale, which could become more relevant for stronger interactions (*31*), cannot be ruled out. In addition, the temperatures before loading into the lattice and after a return to the dipole trap with a reversed sequence were compared. We found a rise in temperature between 0.010(5) T/T_F for a noninteracting cloud and 0.05(2) T/T_F for a medium repulsion of $U/12J = 1$ at compressions around $E_t/12J \approx 0.5$. The good agreement between the experimental data and the numerical calculations, which assume adiabatic loading and an initial temperature of $T/T_F = 0.15$, indicates that our actual initial temperatures lie rather at the lower end of the measured temperature range $T/T_F = 0.15(3)$.

The theoretical calculations of the compressibility shown in Fig. 4D demonstrate that the minimum in the local compressibility, which signals the Mott insulating state, starts to form at initial temperatures in the range of $0.15 \lesssim T/T_F \lesssim 0.2$. At these temperatures, the entropy per particle is much higher than is possible in a Mott insulator in the homogeneous case ($< k_B \ln 2$; where k_B denotes Boltzmann's constant) and even exceeds the maximum possible entropy per particle of a half-filled homogeneous Hubbard model ($k_B \ln 4$). In the trap, however, a large fraction of the entropy is accumulated in the metallic shells at the edges of the atomic cloud where the diluted atoms have a large configurational entropy (fig. S5). Therefore, the temperature remains on the order of $k_B T_{lat} \simeq J \ll U$ in the Mott insulating regime (fig. S4). This is similar to the results obtained in recent calculations and experiments on the melting of incompressible bosonic Mott insulating shells at increasing temperatures (*32*, *33*).

Lattice occupation. In addition to the global compressibility measurements, the fraction of atoms on doubly occupied lattice sites (pair fraction p) was measured for magnetic fields above the Feshbach resonance ($U/12J = 0, 0.5, 1$) by converting all atoms on doubly occupied sites into molecules using a magnetic field ramp (0.2 ms/G) over the Feshbach resonance (*16*, *21*). To prevent tunneling of the atoms during the field ramp, the lattice depth was further increased to 20 E_r in 200 μs. After the ramp, the lattice depth was linearly decreased to zero in 200 μs and the number of remaining atoms was recorded by time-of-flight absorption imaging, yielding the number of singly occupied lattice sites. The difference in atom number with and without the magnetic field ramp normalized to the total atom number gives the desired fraction p, which is plotted in Fig. 5, including corrections for atom losses during the measurement sequence (*14*). The fraction of atoms on doubly occupied sites gives insight into the local onsite physics of the system. In combination with the in situ size measurements, this fraction can be compared for different interaction strengths at constant cloud size R_{sc}.

In the limit of weak confinement, the cloud is large and p tends to zero, regardless of interaction. For intermediate compressions, the fraction of doubly occupied sites depends crucially on the interaction. At a constant size $R_{sc} = 0.53$, we find a pair fraction of 40% for a noninteracting cloud and of around 5% for an intermediate repulsive interaction $U/12J = 1$ (yellow circles in Fig. 5). In this regime of repulsive interactions, it is energetically favorable to reduce the number of doubly occupied sites despite the cost in potential and kinetic energy. As a consequence, different compressions are needed to reach the same system size for different interactions (Fig. 3).

For strong compressions, the measured pair fraction becomes comparable for all interactions (Fig. 5), because all atom distributions are expected to contain a large band-insulating core (figs. S8 and S9). Ultimately, the pair fraction is limited to <60% because of the finite entropy per particle, which reduces the filling factor in the band-insulating state. Although the noninteracting and the slightly repulsively interacting curve $U/12J = 0.5$ match the DMFT results for an inital temperature of $T/T_F = 0.15$, we see deviations for stronger repulsive interactions ($U/12J = 1$). In this case, the measured pair fraction is in general ~10% higher than predicted by theory; nevertheless, the qualitative behavior agrees very well. In general, a suppressed pair fraction in comparison with the noninteracting case, which was also measured in (*16*), occurs for all temperatures in the lattice below $k_B T_{lat} \approx U$, regardless of the formation of an incompressible Mott insulating phase in the inhomogeneous system (fig. S3). Furthermore, the pair fraction vanishes even for a compressible purely metallic phase with $n_{i,\sigma} < 1/2$ in the strongly interacting regime.

Conclusion and outlook. We have determined the global compressibility of repulsively interacting fermionic atoms in an optical lattice and have explored the different regimes from a Fermi liquid to a Mott and band-insulating state when harmonic confinements and interactions were increased. We find good agreement with the results predicted by DMFT.

Our measurements present an important step in the direction of analyzing fermionic many-body systems with repulsive interactions in a lattice. For initial entropies lower than $S/N \lesssim k_B \ln 2$, one expects the system to enter an antiferromagnetically ordered phase, because the temperature of the quantum gas can then drop below the superexchange coupling that mediates an effective spin-spin interaction between the particles (*20*, *30*, *34*, *35*). This would open the path to the investigation of quantum magnetism with ultracold atoms (*36*), being an encouraging starting point from which to ultimately determine the low-temperature phase diagram of the Hubbard model (*1*, *37*). This includes the search for a d-wave superconducting phase (*38*) that is believed to emerge from within the 2D Hubbard model.

References and Notes

1. P. Lee, N. Nagaosa, X.-G. Wen, *Rev. Mod. Phys.* **78**, 17 (2006).
2. J. Hubbard, *Proc. R. Soc. London Ser. A* **276**, 238 (1963).
3. F. Gebhard, *The Mott Metal-Insulator Transition—Models and Methods* (Springer, New York, 1997).
4. D. Jaksch, P. Zoller, *Ann. Phys. (N.Y.)* **315**, 52 (2005).
5. I. Bloch, J. Dalibard, W. Zwerger, *Rev. Mod. Phys.* **80**, 885 (2008).
6. M. P. A. Fisher, P. B. Weichman, G. Grinstein, D. S. Fisher, *Phys. Rev. B* **40**, 546 (1989).
7. D. Jaksch, C. Bruder, J. I. Cirac, C. W. Gardiner, P. Zoller, *Phys. Rev. Lett.* **81**, 3108 (1998).
8. M. Greiner, M. O. Mandel, T. Esslinger, T. Hänsch, I. Bloch, *Nature* **415**, 39 (2002).
9. T. Stöferle, H. Moritz, C. Schori, M. Köhl, T. Esslinger, *Phys. Rev. Lett.* **92**, 130403 (2004).
10. I. B. Spielman, W. D. Phillips, J. V. Porto, *Phys. Rev. Lett.* **98**, 080404 (2007).
11. P. W. Anderson, *Phys. Rev.* **109**, 1492 (1958).
12. J. Billy *et al.*, *Nature* **453**, 891 (2008).
13. G. Roati *et al.*, *Nature* **453**, 895 (2008).
14. See supporting material on *Science* Online.
15. F. Gerbier, S. Fölling, A. Widera, O. Mandel, I. Bloch, *Phys. Rev. Lett.* **96**, 090401 (2006).
16. R. Jördens, N. Strohmaier, K. Günter, H. Moritz, T. Esslinger, *Nature* **455**, 204 (2008).
17. A. Georges, G. Kotliar, W. Krauth, M. J. Rozenberg, *Rev. Mod. Phys.* **68**, 13 (1996).
18. G. Kotliar, D. Vollhardt, *Phys. Today* **57**, 53 (2004).
19. R. W. Helmes, T. A. Costi, A. Rosch, *Phys. Rev. Lett.* **100**, 056403 (2008).
20. L. De Leo, C. Kollath, A. Georges, M. Ferrero, O. Parcollet, http://arxiv.org/abs/0807.0790v1.
21. C. A. Regal, C. Ticknor, J. L. Bohn, D. S. Jin, *Nature* **424**, 47 (2003).
22. This heating can be caused by a p-wave Feshbach resonance for $\left|\frac{9}{2}, -\frac{7}{2}\right\rangle$ atoms at 199 G. Alternatively, we have tried to use a mixture of $\left|\frac{9}{2}, -\frac{9}{2}\right\rangle$ and $\left|\frac{9}{2}, -\frac{5}{2}\right\rangle$ atoms (*16*). However, this mixture showed large losses due to a coupling to the same p-wave channel, for which two-body loss coefficients in excess of 10^{-12} cm^3 s^{-1} have been reported for collisional energies of $E/k_B \simeq 1$ μK. Collisional energies in excess of 1 μK are reached on a lattice site, due to the tight confinement of two atoms and the resulting large zero-point energy.
23. M. R. Andrews *et al.*, *Science* **273**, 84 (1996).
24. A. Kastberg, W. D. Phillips, S. L. Rolston, R. J. C. Spreeuw, P. S. Jessen, *Phys. Rev. Lett.* **74**, 1542 (1995).
25. M. Greiner, I. Bloch, M. O. Mandel, T. Hänsch, T. Esslinger, *Phys. Rev. Lett.* **87**, 160405 (2001).
26. M. Köhl, H. Moritz, T. Stöferle, K. Günter, T. Esslinger, *Phys. Rev. Lett.* **94**, 080403 (2005).
27. R. Bulla, T. A. Costi, D. Vollhardt, *Phys. Rev. B* **64**, 045103 (2001).
28. R. Bulla, T. A. Costi, T. Pruschke, *Rev. Mod. Phys.* **80**, 395 (2008).
29. R. W. Helmes, T. A. Costi, A. Rosch, *Phys. Rev. Lett.* **101**, 066802 (2008).
30. F. Werner, O. Parcollet, A. Georges, S. R. Hassan, *Phys. Rev. Lett.* **95**, 056401 (2005).
31. K. Winkler *et al.*, *Nature* **441**, 853 (2006).
32. F. Gerbier, *Phys. Rev. Lett.* **99**, 120405 (2007).
33. S. Fölling, A. Widera, T. Müller, F. Gerbier, I. Bloch, *Phys. Rev. Lett.* **97**, 060403 (2006).
34. A. Koetsier, R. Duine, I. Bloch, H. Stoof, *Phys. Rev. A* **77**, 023623 (2008).
35. M. Snoek, I. Titvinidze, C. Toke, K. Byczuk, W. Hofstetter, *N. J. Phys.* **10**, 093008 (2008).
36. M. Lewenstein *et al.*, *Adv. Phys.* **56**, 243 (2007).
37. W. Hofstetter, J. I. Cirac, P. Zoller, E. Demler, M. D. Lukin, *Phys. Rev. Lett.* **89**, 220407 (2002).

38. S. Trebst, U. Schollwöck, M. Troyer, P. Zoller, *Phys. Rev. Lett.* **96**, 250402 (2006).
39. We thank E. Demler for fruitful discussions; T. Rom, D. van Oosten, and S. Braun for help during the setup of the experiment; and the Leibniz Institute of Surface Modification (IOM Leipzig) for providing the phase masks used in phase-contrast imaging. We acknowledge funding by the Deutsche Forschungsgemeinschaft (grants FOR801, SFB608, and SFB TR 12), European Union (Scalable Quantum Computing with Light and Atoms), Air Force Office of Scientific Research, and Defense Advanced Research Projects Agency (Optical Lattice Emulator), as well as supercomputer support by the John von Neumann Institute for Computing (Jülich). S.W. acknowledges additional support by MATCOR.

Supporting Online Material
www.sciencemag.org/cgi/content/full/322/5907/1520/DC1
SOM Text
Figs. S1 to S8
References

3 September 2008; accepted 20 October 2008
10.1126/science.1165449

Attosecond Ionization and Tunneling Delay Time Measurements in Helium

P. Eckle,[1] A. N. Pfeiffer,[1] C. Cirelli,[1] A. Staudte,[2] R. Dörner,[3] H. G. Muller,[4] M. Büttiker,[5] U. Keller[1]

It is well established that electrons can escape from atoms through tunneling under the influence of strong laser fields, but the timing of the process has been controversial and far too rapid to probe in detail. We used attosecond angular streaking to place an upper limit of 34 attoseconds and an intensity-averaged upper limit of 12 attoseconds on the tunneling delay time in strong field ionization of a helium atom. The ionization field derives from 5.5-femtosecond-long near-infrared laser pulses with peak intensities ranging from 2.3×10^{14} to 3.5×10^{14} watts per square centimeter (corresponding to a Keldysh parameter variation from 1.45 to 1.17, associated with the onset of efficient tunneling). The technique relies on establishing an absolute reference point in the laboratory frame by elliptical polarization of the laser pulse, from which field-induced momentum shifts of the emergent electron can be assigned to a temporal delay on the basis of the known oscillation of the field vector.

The tunneling process is one of the primary manifestations of quantum mechanics' departure from classical physics. However, the question of whether tunneling through an energetically forbidden region takes a finite time or is instantaneous has been subject to ongoing debate over the past 60 years (*1*). Recently, experimental investigations of atomic interactions with intense laser fields (*2*, *3*) have failed to offer a definitive answer, and many different theoretical predictions seem to contradict each other (*4*–*7*).

Ionization of an atom in a strong laser field allows for addressing this question of a possible tunneling time in an experimentally and conceptually well-defined manner. The strong-field ionization process can be split in two distinct steps: First, the bound electron tunnels through the potential wall created by the superposition of the atomic Coulomb potential and the laser field. After tunnel ionization, the electron is usually treated as a free electron with zero initial kinetic energy at the exit of the tunnel. In the second step, the now-free electron is accelerated by the laser field and receives a linear drift momentum that only depends on the laser field strength at the time of tunneling. This is in strong analogy to the three-step model in high harmonic generation (*8*) using linearly polarized light.

In our experiment, we used close-to-circular polarization, thereby ensuring a unique relationship between the time at which the electron exits the tunnel and the direction of its momentum after the laser pulse. The measured momentum vector of the electron hence serves as the hand of a clock, indicating the time when the electron appeared from the tunnel in the laser field. The clock face is determined by the rotating electric field of the close-to-circularly polarized laser pulse. Thus, if we know the direction of laser field at time zero, $t_{0,\mathrm{field}}$, when the tunneling process is initiated, we can determine the time the electron has spent in the tunnel in the classically forbidden region inside the potential wall. This difference or delay we refer to as the tunneling delay time, Δt_D.

The high-field ionization process exhibits different regimes that are distinguished by the Keldysh parameter, γ, which is given for circularly polarized light by (*9*)

$$\gamma = \frac{\omega_0\sqrt{2I_p}}{E_0}(\text{atomic units}) \cong 0.327\sqrt{\frac{I_p(\text{eV})}{I_0(10^{14}\text{W/cm}^2)[\lambda(\mu\text{m})]^2}} \quad (1)$$

where I_p is the ionization potential, ω_0 the center laser angular frequency, E_0 the electric field amplitude of the intense infrared (IR) laser pulse, I_0 the peak intensity of the pulse, and λ the laser wavelength. For example, for the helium ionization potential of 24.59 eV, a peak intensity of 10^{14} W/cm^2, and a center wavelength of 725 nm, we obtain $\gamma = 2.24$ for circular polarization (Eq. 1). For the same peak intensity, γ is a factor of $\sqrt{2}$ larger for circularly polarized light than for linearly polarized light. For $\gamma \gg 1$, that is, for short wavelength and low intensity, the ionization is most properly described by the simultaneous absorption of many discrete photons. On the other hand, if $\gamma \ll 1$, tunneling of the bound electron through a classical potential barrier provides the appropriate physical picture of the ionization process. The two regimes are not expected to be separated by a sharp transition, and both tunneling and multiphoton ionization contribute in the intermediate regime with $\gamma \approx 1$. Recently this intermediate regime was referred to as the regime of nonadiabatic tunneling (*12*). So far, all high laser field experiments have confirmed that, in this intermediate regime, the tunnel ionization is the dominant process, fully explaining, for example, high harmonic generation (*8*), quantum path interferences (*10*), and laser-induced electron tunneling and diffraction (*11*). A simple tunneling time was introduced by Keldysh (*9*) and more recently extended to the nonadiabatic tunneling regime (*12*), which formally agrees with the Büttiker-Landauer traversal time for tunneling, Δt_T (*9*, *13*):

$$\gamma = \omega_0\Delta t_T \Rightarrow \Delta t_T(\text{as}) = 0.531\cdot\gamma\cdot\lambda(\mu\text{m}) = 0.174 \times \sqrt{\frac{I_p(\text{eV})}{I_0(10^{14}\text{W/cm}^2)}} \quad (2)$$

We have experimentally explored the nonadiabatic tunneling regime in helium atoms exposed to laser fields with γ ranging from 1.45 to 1.17 corresponding to a peak intensity ranging from 2.3×10^{14} to 3.5×10^{14} W/cm^2 (Eq. 1), which in turn corresponds to a Δt_T between 450 to 560 as. At these intensities, over-the-barrier ionization (*14*) is negligible because for helium the critical intensity is $\approx 1 \times 10^{15}$ W/cm^2 (i.e., $\gamma = 0.71$ for circular polarization and $\lambda = 725$ nm).

Close-to-circularly polarized pulses with a duration in the two optical cycle regime (5.5 fs) and a center wavelength of 725 nm, which were produced by a Ti:Sapphire based laser system and a two-stage filament compressor (*15*), were focused onto helium atoms inside a COLTRIMS apparatus (*16*). Instead of measuring the electron momentum distributions directly, we recorded helium ion distributions. Momentum conservation

[1]Physics Department, Eidgenössische Technische Hochschule (ETH) Zürich, CH-8093 Zürich, Switzerland. [2]Steacie Institute for Molecular Sciences, National Research Council of Canada, 100 Sussex Drive, Ottawa, Ontario K1A 0R6, Canada. [3]Institut für Kernphysik, Johann Wolfgang Goethe Universität, Max-von-Laue-Straße 1, 60438 Frankfurt am Main, Germany. [4]Stichting voor Fundamenteel Onderzoek der Materie–Institute for Atomic and Molecular Physics, Kruislaan 407, 1098 SJ Amsterdam, Netherlands. [5]Physics Department, University of Geneva, CH-1211 Geneva, Switzerland.